

# Electrodeposited Manganese Oxide on Carbon Paper for Zinc-Ion Battery Cathodes

Arjun Dhiman<sup>[a]</sup> and Douglas G. Ivey<sup>\*[a]</sup>

Nano-crystalline, flake-like Mn oxide was electrodeposited onto carbon paper (CP) using a pulsed electrodeposition technique. The electrodeposited Mn oxide was identified as  $Mn_3O_4$  through a combination of X-ray photoelectron spectroscopy (XPS), X-ray diffraction (XRD), and Raman spectroscopy. The  $Mn_3O_4$  on CP was used as a cathode for Zn-ion batteries (ZIBs) and showed excellent cyclability at a current density of  $1\text{ A g}^{-1}$  with a capacity retention of 139% after 200 cycles. Electron microscopy was used to characterize the microstructural changes of

the cathode at various stages during discharge/charge cycling. This work in combination with the electrochemical results suggests a two-step reaction mechanism involving both intercalation and conversion reactions. The results demonstrate that electrodeposition of the cathode material is a simple, quick, and potentially scalable electrode synthesis method for producing high performing Zn-ion electrodes without the use of binders or other additives.

## 1. Introduction

While Li-ion batteries (LIBs) dominate the battery market from portable electronics to vehicles, they face several challenges that limit their future application, such as limited resources for battery materials, cost, and safety concerns.<sup>[1,2]</sup> In the literature, there has been increased interest recently in Zn-ion batteries (ZIBs) as a replacement for LIBs. This is largely attributed to the low cost, abundance, high theoretical capacity ( $820\text{ mAh g}^{-1}$ ), compatibility with aqueous and non-aqueous electrolytes, and the low environmental impact of Zn.<sup>[1,3]</sup> However, ZIBs face several challenges that have restricted their implementation as an alternative to LIBs. In general, ZIB cathode materials have limited capacities, poor capacity retention, poor rate capabilities, limited potential windows, low operating potentials, or a combination of the aforementioned issues.<sup>[1,4,5]</sup>

Presently, several different categories of materials have been explored for use as cathodes, with the most popular ones being V oxide compounds,<sup>[4–14]</sup> Prussian blue analogues (PBA),<sup>[4,5,15–18]</sup> and Mn oxide compounds.<sup>[4,5,19–35]</sup> To a lesser extent, sustainable quinone analogs, metal sulfides, Chevrel phase compounds, and polyanion based compounds have also been explored.<sup>[4,5,36]</sup> Of the different materials explored for ZIB cathodes, the most commonly studied material is Mn oxide. This is in large part due to Mn oxide's large theoretical capacity, non-toxicity, abundance, numerous stable valence states, and low cost.<sup>[5,36]</sup> Of the different Mn oxide phases that have been studied, there have only been a handful of instances where

$Mn_3O_4$  has been used as a cathode material for ZIBs.<sup>[24–26,31,32,34]</sup>  $Mn_3O_4$  has been extensively studied for Zn-air batteries and has been shown to be a good oxygen reduction reaction (ORR) catalyst for the air electrode in Zn-air batteries.<sup>[37,38]</sup>

Currently, there are still many issues associated with the use of  $Mn_3O_4$  as an electrode for ZIBs that must be addressed if ZIBs are to become a widely accepted technology. Like other Mn oxide compounds,  $Mn_3O_4$  experiences severe capacity fade, poor rate capabilities, low capacities, or a combination of these. These issues have generally been associated with cathode material phase change upon cycling, Mn dissolution, poor Mn oxide conductivity, or the formation of reaction side products.<sup>[25,31,32]</sup> Dissolution of Mn is generally addressed by the addition of Mn into the electrolyte, while poor conductivity is minimized by the use of carbon additives or conductive substrates.<sup>[25,26,28,32,36]</sup> Recently, Fang et al. have shown that the incorporation of K into the cathode can also help suppress Mn dissolution.<sup>[39]</sup> Reducing particle size and increasing surface area of the active material has also been employed to address the poor conductivity of Mn oxides.<sup>[33]</sup> Furthermore, the reaction mechanism surrounding  $Mn_3O_4$  materials, and Mn oxide compounds in general, is still not completely understood. In the literature, many groups have argued that Mn oxide materials undergo Zn intercalation during battery cycling, with both discharge plateaus corresponding to Zn insertion into different sites within the cathode structure.<sup>[40–42]</sup> However, other groups contend that Mn oxides undergo a chemical conversion reaction.<sup>[28]</sup> There have also been reports of a co-intercalation process, where  $H^+$  insertion occurs in the first plateau followed by  $Zn^{2+}$  insertion during the second plateau.<sup>[30,43]</sup> More recently, Chao et al. have proposed a fourth mechanism involving the deposition and dissolution of  $MnO_2$  for ZIBs.<sup>[44]</sup> The battery uses an electrolyte consisting of  $H_2SO_4$ ,  $ZnSO_4$ , and  $MnSO_4$ . Zinc in the battery undergoes a plating and stripping reaction at the anode, but Zn is not directly involved in the cathode processes. Regarding  $Mn_3O_4$  in particular, Hao et al. have suggested that  $Mn_3O_4$  undergoes a co-intercalation mechanism during dis-

[a] A. Dhiman, Prof. D. G. Ivey  
Department of Chemical and Materials Engineering  
University of Alberta,  
Edmonton Alberta, Canada T6G 1H9  
E-mail: divey@ualberta.ca

 Supporting information for this article is available on the WWW under  
<https://doi.org/10.1002/batt.201900150>

 An invited contribution to a Special Collection dedicated to the Symposium on Batteries and Supercapacitors at the E-MRS Spring Meeting 2019

charge with  $\text{H}^+$  insertion followed by  $\text{Zn}^{2+}$  insertion.<sup>[31]</sup> They also mention that zinc sulfate hydroxide (ZSH or  $\text{Zn}_4(\text{OH})_6(\text{SO}_4)_5 \cdot 5\text{H}_2\text{O}$ ) and manganese oxyhydroxide ( $\text{MnOOH}$ ) form during battery discharge but are dissolved on recharge. Additionally, during the initial charge, Hao et al. propose that  $\text{Mn}_3\text{O}_4$  is converted to  $\text{Mn}_5\text{O}_8$  and birnessite ( $\delta\text{-MnO}_2$ ) with no  $\text{Zn}^{2+}$  involved in this process. On the other hand, Zhu et al. propose that  $\text{Mn}_3\text{O}_4$  undergoes a chemical conversion reaction with  $\text{Mn}_3\text{O}_4$  transforming to  $\text{MnO}$  on discharge, accompanied by the formation of large plate-like ZSH.<sup>[32]</sup> During recharge, ZSH is dissolved and  $\text{MnO}$  is converted back to  $\text{Mn}_3\text{O}_4$ .  $\text{ZnMn}_2\text{O}_4$  is another spinel structure that has been explored for ZIBs. Zhang et al. and Wu et al. have both proposed that  $\text{ZnMn}_2\text{O}_4$  undergoes  $\text{Zn}^{2+}$  intercalation/deintercalation reactions for discharge and charge, without any phase transformation or formation of any side products.<sup>[24,25]</sup> Yang et al. used a combined  $\text{ZnMn}_2\text{O}_4$  and  $\text{Mn}_2\text{O}_3$  cathode and also proposed that the material only underwent  $\text{Zn}^{2+}$  intercalation during cycling.<sup>[34]</sup> However, Chen et al. have reported that the formation of ZSH accompanies  $\text{Zn}$  intercalation during  $\text{ZnMn}_2\text{O}_4$  cycling.<sup>[26]</sup>

Hydrothermal methods are commonly used to fabricate the cathode material. This involves keeping the reactants at elevated temperatures and pressures in an autoclave for several hours.<sup>[25,32]</sup> The produced cathode material is ground and combined with carbon black and a binder to create a slurry that is cast onto a substrate. The electrode is then heated for several hours for drying, followed by a sintering step before it is ready for use.<sup>[24,34]</sup> The entire fabrication process can easily take more than 24 h to generate a sample. The use of a slurry method to apply the produced material to the substrate can result in significant variations in mass loading from sample to sample.<sup>[28]</sup> Solution precipitation methods, in combination with the slurry method, can also take a similar length of time to prepare the active material and electrodes for ZIBs.<sup>[31]</sup> Electrodeposition is a fast, simple, and inexpensive one-step technique that can deposit a wide variety of materials. This technique works by depositing solvated ionic species onto a conductive substrate by applying an external potential or current.<sup>[45]</sup> The simplicity of electrodeposition allows for fast turnaround for material deposition and testing, which is beneficial when considering scalability. Additionally, electrodeposition is easily reproducible resulting in highly consistent deposits. With electrodeposition, the active cathode materials for ZIBs can be directly deposited onto an electrode substrate at room temperature without the requirement of binders and lengthy fabrication times. Electrodeposition has been utilized previously in the literature to fabricate Mn oxide cathode materials for ZIBs.<sup>[30,46,47]</sup> Sun et al. used a potentiostatic method to deposit  $\text{MnO}_2$  onto carbon fiber paper (CFP), which was then employed in a battery with an electrolyte consisting of 2 M  $\text{ZnSO}_4$  and 0.2 M  $\text{MnSO}_4$ .<sup>[30]</sup> Li et al. utilized a galvanostatic method to deposit  $\text{MnO}_2$  onto carbon electrodes with a battery electrolyte composed of 1 M  $\text{ZnSO}_4$  and 0.2 M  $\text{MnSO}_4$ .<sup>[47]</sup>

In this study Mn oxide is electrochemically deposited onto carbon paper (CP) via a pulsed electrodeposition technique for use as a cathode for ZIBs. The deposited oxide is identified through a number of microstructural characterization techni-

ques as  $\text{Mn}_3\text{O}_4$ . As such the oxide is hereafter referred to as  $\text{Mn}_3\text{O}_4$ . Electrode fabrication can be done in ~1 h and does not require the use of binders. The process should also be easily scalable to produce ZIB cathode materials. The  $\text{Mn}_3\text{O}_4$ -based cathode demonstrates good rate capability and cycling performance during ZIB testing. Furthermore, insight into the reaction mechanisms associated with discharging and charging of  $\text{Mn}_3\text{O}_4$ -based materials is provided.

## Experimental Section

### Material Synthesis and Electrode Preparation

The electrodeposition technique used is similar to that reported by Xiong et al. to fabricate air electrodes for zinc-air batteries.<sup>[37]</sup> To summarize, anodic pulsed electrodeposition was employed at an applied current of 4.7 mA with a 0.25 s ON cycle and a 0.5 s OFF cycle, for a total of 2400 cycles. The electrolyte solution consisted of 0.02 M of  $\text{Mn}(\text{CH}_3\text{COO})_2$ , 100 mg  $\text{L}^{-1}$  of sodium dodecyl sulfide (SDS), and 0.02 M of  $\text{NaCH}_3\text{COO}$ . Flexible carbon paper (CP, Freudenberg H23C6) and Pt mesh were used as the working electrode and counter electrode, respectively. The nominal deposition area was 4  $\text{cm}^2$ . During the deposition process, the electrodeposition cell was placed in an ultrasonic bath (Branson 2510, 40 kHz) to agitate the solution. Once the Mn oxide was deposited onto the CP, the material was rinsed with deionized water and then annealed for 30 min at 300 °C to help increase the oxidation state of the material and improve the crystallinity. The mass loading of the  $\text{Mn}_3\text{O}_4$  was ~0.3–0.4 mg  $\text{cm}^{-2}$  on the CP substrate.

### Material Characterization

Scanning electron microscopy (Tescan Vega3 SEM, operated at 20 kV) and energy dispersive X-ray spectroscopy (EDX) were used to characterize the microstructure and composition of the fabricated samples. Samples for SEM were prepared by mounting the cathode to Al stubs using carbon tape. Transmission/scanning transmission electron microscopy (JEOL JEM-ARM200CF TEM/STEM, operated at 200 kV) and EDX mapping were also used to examine the microstructure and composition of the sample at higher magnifications, as well as to generate crystal structure information. TEM samples were prepared by scraping the deposited  $\text{Mn}_3\text{O}_4$  from the CP and dispersing the powder in 1 mL of ethanol, while agitating in an ultrasonic bath. One or two drops of the suspension were placed onto holey carbon coated grids using a pipette and then the ethanol was allowed to evaporate. Oxidation states of the components in the samples were examined using X-ray photoelectron spectroscopy (XPS), which was conducted using a monochromatic  $\text{Al K}_{\alpha}$  X-ray source with a pass energy of 20 eV (Kratos AXIS Supra XPS Instrument). The collected XPS spectra were calibrated using the C 1s peak at 284.8 eV and analyzed using Casa XPS software. X-ray diffraction (XRD) was also utilized to examine the crystal structure of the samples with a  $\text{Co K}_{\alpha}$  ( $\lambda = 0.179 \text{ nm}$ ) X-ray source (Rigaku Ultima IV). The patterns were collected in powder mode and converted to a Cu source using JADE 9.6 software for easy comparison with PDF cards. Raman scattering spectroscopy (Thermo DXR2 Raman microscope) was used to help in identifying the type of metal oxide deposited. Spectra were obtained between 100 and 1000  $\text{cm}^{-1}$  at room temperature using an excitation energy of 532 nm<sup>-1</sup>. Each Raman spectrum collected was an average of 20 scans to help improve the signal to noise ratio.

## Electrochemical Measurements and Battery Testing

Electrochemical testing was done using a Biologic SP-300 potentiostat with CR 2032-coin cells. The coin cells were assembled using  $\text{Mn}_3\text{O}_4$  on CP as the working electrode, Zn foil as the counter electrode, and a glass fiber separator. A solution of 2 M  $\text{ZnSO}_4$  + 0.2 M  $\text{MnSO}_4$  was used as the electrolyte. Cyclic voltammetry (CV) and galvanostatic charge and discharge (GCD) tests were done in a potential window between 1.0 and 1.8 V. A scan rate of  $0.1 \text{ mV s}^{-1}$  was applied for CV testing. Several different applied current densities were used for GCD testing, ranging from  $300 \text{ mA g}^{-1}$  to  $2.4 \text{ A g}^{-1}$ . The applied current densities were normalized to the mass of  $\text{Mn}_3\text{O}_4$  on the electrode. All tests were done at room temperature and were IR-corrected.  $\text{Zn}/\text{Zn}^{2+}$  was used as the reference electrode for all electrochemical testing.

## 2. Results and Discussion

### 2.1. Material Characterization Results

The SEM images presented in Figure 1a and b show the pristine as deposited  $\text{Mn}_3\text{O}_4$  on CP.  $\text{Mn}_3\text{O}_4$  forms islands on the CP and the islands have a flake-like morphology. This flake-like morphology provides a high surface area for exposure to the electrolyte. Additionally, from the higher magnification inset SEM image (Figure 1b), the  $\text{Mn}_3\text{O}_4$  islands have a thickness of  $\sim 1\text{--}2 \mu\text{m}$ . A high surface area coupled with a thin deposit can improve ZIB performance by reducing the distance electrons need to travel, thus counteracting the relatively poor conductivity of Mn oxides. STEM EDX mapping confirms that the

deposit mainly consists of Mn and O (Figure 1d–1g). A small amount of S is also present, which is likely from the SDS used as an additive in the electrodeposition solution. The high resolution TEM image (Figure 1h) shows that the deposited  $\text{Mn}_3\text{O}_4$  oxide is nanocrystalline in nature with grains measuring roughly 5 nm in size. The inset image in Figure 1h shows a magnified view of the region indicated. Lattice spacings of 0.27 nm and 0.30 nm correspond to the (220) and (113) planes, respectively, of cubic  $\text{Mn}_3\text{O}_4$  (113) plane; however, they could correlate with the (200) and (013) planes of tetragonal  $\text{Mn}_3\text{O}_4$  (hausmannite) as well.

XPS analysis was carried out to ascertain the oxidation state of the Mn in the Mn oxide deposit. Using the area of the Mn 2p satellite features (Figure 2a), the average oxidation state of the deposited material was determined to be roughly 2.55, which is close to that of  $\text{Mn}_3\text{O}_4$  (2.67).<sup>[48,49]</sup> Furthermore, the Mn 3s peak splitting (Figure 2b) was determined to be 5.54 eV, which is very similar to the 5.50 eV Mn 3s peak splitting expected for  $\text{Mn}_3\text{O}_4$ .<sup>[48,49]</sup> In addition, the difference between the Mn 2p 3/2 and O 1s peak energies also suggests that the deposit could be  $\text{Mn}_3\text{O}_4$ .<sup>[48]</sup> Finally, the survey scan for the deposit (Figure S1) was used to estimate the relative atomic amounts of the detected elements, giving  $\sim 45$  at% Mn and 55 at% O, which are close to composition corresponding to  $\text{Mn}_3\text{O}_4$ . A summary of the XPS analysis for the deposited  $\text{Mn}_3\text{O}_4$  is given in Table 1, along with comparisons with other Mn oxides.

An XRD pattern of the deposited Mn oxide is presented in Figure 2c. The pattern was obtained by scraping off the deposit from the CP and placing the powder on a zero-background

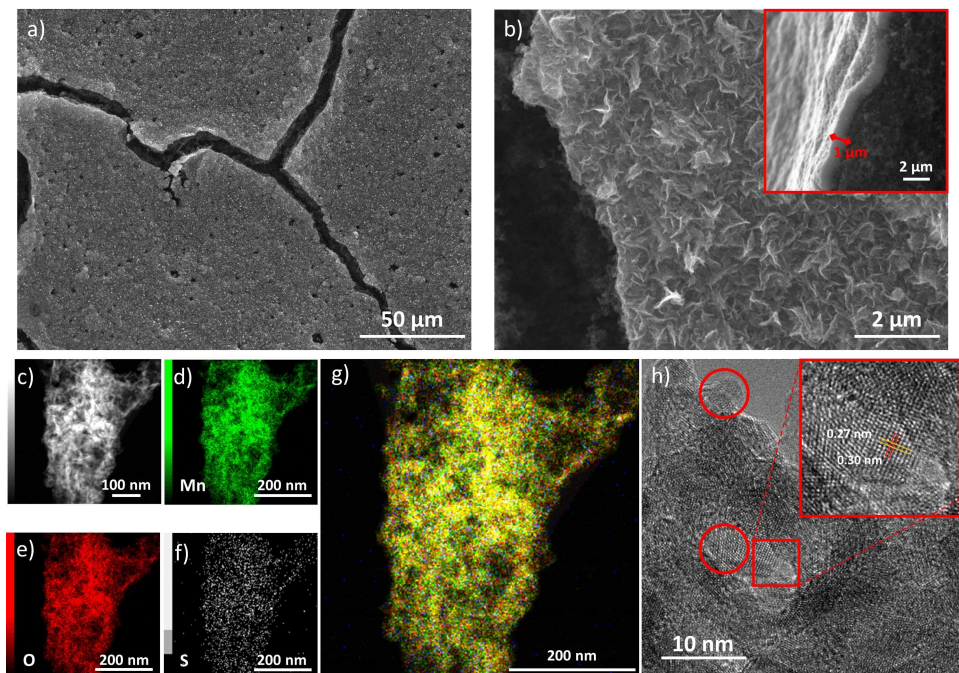


**Figure 1.** Electron microscopy analysis of as-deposited  $\text{Mn}_3\text{O}_4$  on CP: a) and b) SEM secondary electron (SE) images showing island formation and flake-like morphology of  $\text{Mn}_3\text{O}_4$ . The inset image in (b) shows a cross section image of the deposit; c) STEM annular dark field (ADF) image of  $\text{Mn}_3\text{O}_4$ ; d–f) EDX maps for Mn, O, and S in the deposit; g) overlaid EDX maps (Mn, O, and S) for  $\text{Mn}_3\text{O}_4$  deposit showing uniform distribution of Mn and O; h) high resolution TEM image depicting nanocrystalline nature of the deposited  $\text{Mn}_3\text{O}_4$  with circles indicating individual particles. The inset image shows the lattice fringes and determined d-spacing.

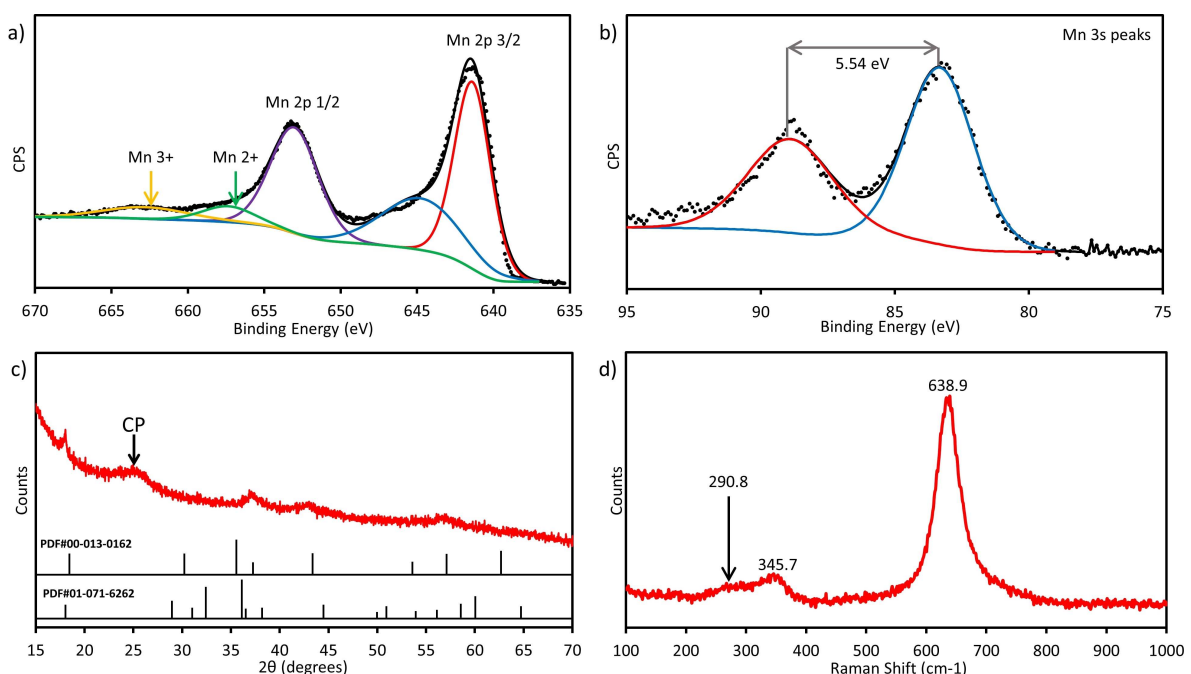


**Figure 2.** Characterization of as deposited Mn<sub>3</sub>O<sub>4</sub>. a) Mn 2p XPS spectrum showing two satellite peaks (labeled Mn 3+ and Mn 2+) used for oxidation state determination. b) Mn 3s XPS spectrum showing the peak splitting used for oxidation state determination. c) XRD pattern and PDF cards for cubic Mn<sub>3</sub>O<sub>4</sub> (PDF#00-013-0162) and hausmannite Mn<sub>3</sub>O<sub>4</sub> (PDF#00-071-6262); the CP peak has been labelled as well. d) Raman spectrum with three peaks labeled.

**Table 1.** Summary of XPS data and comparison with other Mn oxide materials.

	Mn (At%)	O (At%)	Mn 2p Avg. Oxidation State	Mn 3s Peak Splitting (eV)	Mn 2p (3/2)/O 1s Binding Energy Difference (eV)
This work	45.3	54.7	2.55	5.54	111.61
Mn <sub>3</sub> O <sub>4</sub> <sup>[48]</sup>	42.9	57.1	2.67	5.50	111.53
Mn <sub>2</sub> O <sub>4</sub> <sup>[48]</sup>	40.0	60.0	3.00	5.41	111.73
MnO <sup>[48]</sup>	50.0	50.0	2.00	5.79	111.29
MnO <sub>2</sub> <sup>[48]</sup>	33.3	66.7	4.00	4.87	112.37

plate. The pattern is not well defined, with weak and broad peaks due to the nanocrystalline nature of the Mn oxide and the limited amount of sample powder. The pattern can be indexed reasonably well to two different Mn<sub>3</sub>O<sub>4</sub> phases, either cubic spinel Mn<sub>3</sub>O<sub>4</sub> (PDF#00-013-0162) or tetragonal hausmannite (PDF#00-071-6262). Hausmannite is the thermodynamically stable form of Mn<sub>3</sub>O<sub>4</sub>. Additionally, the XRD pattern is similar to the pattern obtained by Zhu et al., who indexed their pattern to hausmannite Mn<sub>3</sub>O<sub>4</sub>.<sup>[32]</sup> The broad peak at ~25–26 degrees is from the CP substrate.

Raman spectroscopy data was collected for the deposited Mn<sub>3</sub>O<sub>4</sub> and is presented in Figure 2d. The spectrum shows one distinct peak at 638.9 cm<sup>-1</sup> and a smaller peak at 345.7 cm<sup>-1</sup>. There may be an additional peak located at 290.8 cm<sup>-1</sup>. This pattern most closely fits with patterns observed for Mn<sub>3</sub>O<sub>4</sub>, further suggesting that the deposit is a Mn<sub>3</sub>O<sub>4</sub>.<sup>[37,50,51]</sup> Therefore, based on the combined XRD, XPS, HR-TEM, and Raman spectroscopy analysis, the electrodeposited Mn oxide is identified as Mn<sub>3</sub>O<sub>4</sub> spinel, likely hausmannite.

## 2.2. Electrochemical Results

Figure 3a shows the CV results for an assembled ZIB using a scan rate of 0.1 mVs<sup>-1</sup>. For the first cathodic and anodic scans, one reduction peak and one oxidation peak occur at 1.18 V and 1.57 V, respectively. On subsequent cycling, two reduction peaks are present at 1.26 V and 1.37 V on the cathodic scan. Two oxidation peaks are also present during the anodic scan at 1.57 V and a small shoulder at ~1.60 V. The CV results show relatively good overlap upon cycling and the CV behaviour is similar to that of other Mn oxide-based ZIBs.<sup>[31,34,36,47]</sup>

Figure 3b shows GCD results obtained for the ZIB. The initial or conditioning cycle was done at a low current density of 50 mA g<sup>-1</sup> to condition or prime the battery before testing, since the initial GCD cycle is different from the subsequent cycles. The subsequent charge and discharge cycles were done at 300 mA g<sup>-1</sup>. The battery has a high initial capacity of 376 mAh g<sup>-1</sup> during the conditioning cycle. At 300 mA g<sup>-1</sup>, the battery has a capacity of 297 mAh g<sup>-1</sup> for the 1<sup>st</sup> cycle and a maximum capacity of 328 mAh g<sup>-1</sup>; the capacity retention is 118% after 100 cycles. During cycling, the discharge plateaus occur at about 1.40 V and 1.30 V and the charge plateaus occur at about 1.52 V and 1.58 V. The peaks from the CV testing correspond well with the plateaus observed during GCD testing, with some variation due to the CV scan rate and applied current density in GCD testing. Additionally, the two pairs of peaks in the CV results and the two plateaus during both charge and discharge indicate a two-step reaction mechanism for the assembled ZIB.

Cycling performance of the battery under an applied load of 1 A g<sup>-1</sup> is presented in Figure 3c. The assembled ZIB has very

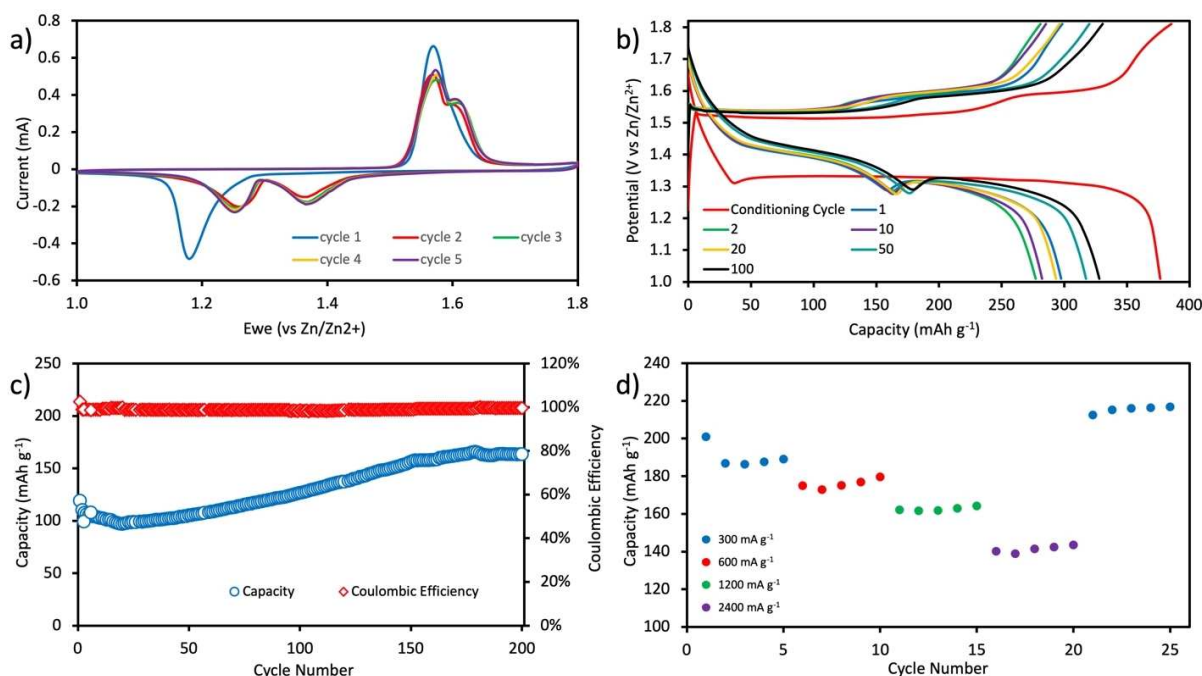


**Figure 3.** Electrochemical and battery performance of assembled ZIB: a) CV results at a scan rate of  $0.1 \text{ mV s}^{-1}$ ; b) GCD testing with the conditioning cycle done at an applied current density of  $50 \text{ mA g}^{-1}$  and the subsequent cycles at  $300 \text{ mA g}^{-1}$ ; c) battery cyclability results at an applied current density of  $1 \text{ A g}^{-1}$ ; d) rate capability test results at various applied current densities.

good performance with a final capacity of  $163 \text{ mAh g}^{-1}$  and a capacity retention of 137% after 200 charge and discharge cycles. The battery capacity also stabilizes toward the end of the cycling. The assembled battery has a Coulombic efficiency close to 100%, indicating good battery reversibility.

The rate capability of the assembled battery was tested as well and is presented in Figure 3d. The  $\text{Mn}_3\text{O}_4$  cathode was cycled 5 times at different current densities and exhibited good rate capability. At 300, 600, 1200, 2400, and then again at  $300 \text{ mA g}^{-1}$ , the battery was able to deliver capacities of 201, 180, 164, 143, and  $217 \text{ mAh g}^{-1}$ , respectively. This also corresponds to a capacity retention of 110% at a current density of  $300 \text{ mA g}^{-1}$  in the GCD test and the rate capability test can be attributed to cathode wettability, gradual activation of the cathode, and sample variation. If the cathode material does not wet properly, the electrolyte may not be in complete contact with the active material, which can reduce battery capacity. Gradual activation of the cathode also affects the capacities in a similar way to wettability. As the cathode cycles, the electrolyte will access more of the active material which will result in an increase in capacity. Additionally, the cathode may not undergo complete activation at higher current density, resulting in reduced initial capacities.<sup>[31]</sup> Improved cathode wettability and gradual cathode material activation may also explain why there is a steady increase in capacity during GCD testing until the capacity stabilizes at close to 200 cycles.<sup>[41,52]</sup> Overall, the good performance of the assembled ZIB can be attributed to several factors. The flake-like morphology of the  $\text{Mn}_3\text{O}_4$  offers a large surface area providing the electrode with better access to the electrolyte.

Also, the  $\text{Mn}_3\text{O}_4$  flakes are very thin ( $\sim 1 \mu\text{m}$ ) and are deposited on a conductive CP substrate, which can help counter the relatively poor conductivity of  $\text{Mn}_3\text{O}_4$ .<sup>[53]</sup> The addition of  $0.2 \text{ M}$   $\text{MnSO}_4$  to the electrolyte provides  $\text{Mn}^{2+}$  ions in the electrolyte, which have been shown to reduce the dissolution of Mn from the electrode and help the electrode and electrolyte reach an equilibrium state.<sup>[25,28]</sup>

Table 2 compares the cycling results for battery testing in this work with those from other batteries using Mn-based spinel cathodes. The batteries from this work either outperform or display comparable performance to other batteries presented in the literature. Galvanostatic intermittent titration testing (GITT) was conducted for the first discharge cycle after conditioning to determine the diffusion coefficient for each plateau (Figure S3). The first plateau shows a smaller potential jump during the rest period versus the second plateau. This indicates that the process occurring during the second plateau has a smaller diffusion coefficient compared with the first plateau and is more kinetically limited.<sup>[30,47,52]</sup>

### 2.3. Reaction Mechanism

The reaction mechanism involving  $\text{Mn}_3\text{O}_4$  and Mn oxide compounds in general, is still widely debated and not completely understood. To gain a better understanding of the electrochemical mechanism, the  $\text{Mn}_3\text{O}_4$  on CP cathode was examined at different stages during charge and discharge for several cycles. In particular, the conditioning cycle, the 1st cycle after conditioning, and the 5th cycle were examined. A current density of  $50 \text{ mA g}^{-1}$  was applied for all cycles for consistency.

**Table 2.** Battery cycling performance comparison between this work and other  $\text{Mn}_3\text{O}_4$  based ZIBs found in the literature.

Cathode material	Electrolyte	Potential window (V)	Current density ( $\text{mA g}^{-1}$ )	Initial capacity ( $\text{mAh g}^{-1}$ )	Final capacity ( $\text{mAh g}^{-1}$ )	Capacity retention	Ref.
$\text{Mn}_3\text{O}_4$	2 M $\text{ZnSO}_4 + 0.2 \text{ M MnSO}_4$	1.0–1.8	1000	119	163	137% after 200 cycles	This work
Stainless-steel@ $\text{Mn}_3\text{O}_4$	2 M $\text{ZnSO}_4 + 0.1 \text{ M MnSO}_4$	1.0–1.8	100	296	290*	98% after 50 cycles	[32]
$\text{ZnMn}_2\text{O}_4$	1 M $\text{ZnSO}_4 + 0.5 \text{ M MnSO}_4$	0.8–1.9	100	86.0	106.5*	124% after 300 cycles*	[25]
$\text{ZnMn}_2\text{O}_4/\text{Mn}_2\text{O}_3$	1 M $\text{ZnSO}_4$	0.8–1.9	500	82.6	111.9*	135% after 300 cycles*	[34]
$\text{Mn}_3\text{O}_4$	2 M $\text{ZnSO}_4$	0.8–1.9	500	45.5*	106.1*	233% after 300 cycles*	[31]
Cation-deficient $\text{ZnMn}_2\text{O}_4$	3 M $\text{Zn}(\text{CF}_3\text{SO}_3)_2$	0.8–2.0	500	~90*	~85*	94% after 500 cycles	[24]
$\text{ZnMn}_2\text{O}/\text{N-doped graphene}$	1 M $\text{ZnSO}_4 + 0.5 \text{ M MnSO}_4$	0.8–1.8	1000	76*	74	97.4% after 2500 cycles	[26]

\* Values were determined from data presented in the specific reference.

For the conditioning cycle, two samples were examined during discharge, at potentials of 1.35 V (pt. 1 on discharge) and 1.25 V (pt. 2 on discharge) and two samples were examined during charge, at potentials of 1.54 V (pt. 1 on charge) and 1.63 V (pt. 2 on charge). These positions correspond to the beginning and end of the discharge plateau and the ends of the two charge plateaus.

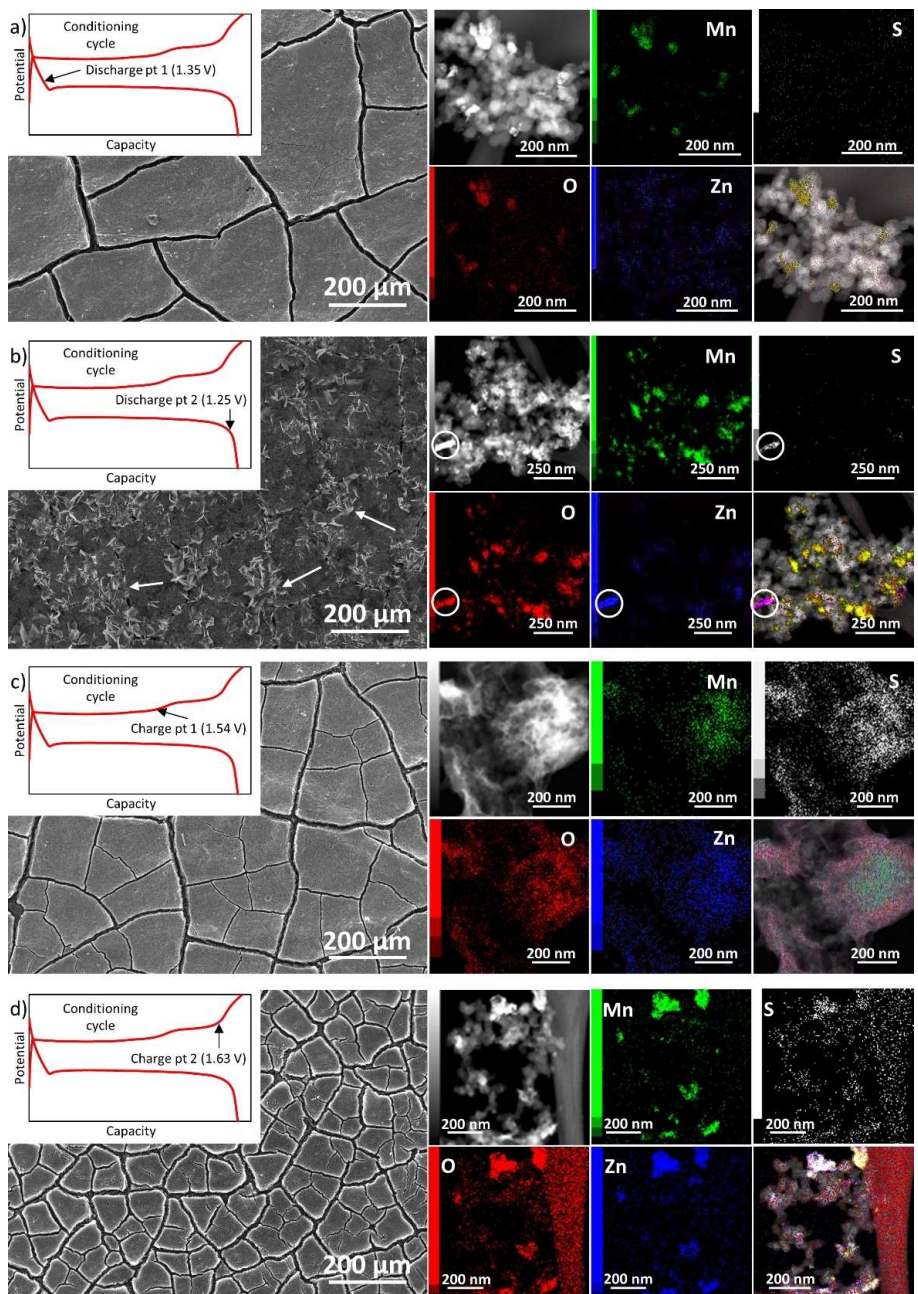
Figure 4 presents SEM images, STEM images and EDX mapping results for discharge and charge during the conditioning cycle. Inset capacity plots associated with the SEM micrographs show where the battery was stopped during the conditioning cycle for examination. The SEM image for the first discharge point at 1.35 V (Figure 4a) shows the morphology of the cathode, which is very similar to the morphology for the pristine sample (Figure 1b). The corresponding STEM image and EDX maps for this sample show carbon particles (~50 nm in size) from the CP, partially covered with Mn oxide particles (bright regions in the STEM annular dark field (ADF) image). Zn is present in this sample, with the Zn map corresponding to the positions of Mn oxide. This result indicates that  $\text{Zn}^{2+}$  intercalation occurs during the first plateau, which is contradictory to several  $\text{Mn}_3\text{O}_4$ , and other Mn oxide, reaction mechanisms reported in the literature that suggest only  $\text{H}^+$  intercalation occurs within the first plateau.<sup>[30,31]</sup>  $\text{H}^+$  intercalation may be occurring simultaneously with the observed  $\text{Zn}^{2+}$  intercalation; however, H is not detectable by EDX and could not be confirmed. There is also a weak EDX signal from S that overlaps with Mn oxide, indicating that some S may be incorporated. The S is likely from the SDS in the electro-deposition solution, as discussed in Section 2.1 and shown in Figure 1. A pristine cathode ( $\text{Mn}_3\text{O}_4$  on CP) was immersed in the electrolyte for several days. Post treatment EDX analysis revealed no Zn, confirming that Zn was not surface absorbed from the electrolyte and is actually incorporated in  $\text{Mn}_3\text{O}_4$  during discharge (Figure S4).

Figure 4b shows a similar set of images and EDX maps to Figure 3a for the cathode examined at the second discharge point (1.25 V). Large plate-like formations, not present in the as deposited sample or the sample from Figure 4a, are present. The plates resemble ZSH that has been reported in the literature to form during discharge of Mn oxide electrodes.<sup>[36,47]</sup> Interestingly, these plates tend to initially form in the areas between the  $\text{Mn}_3\text{O}_4$  islands on the CP and so the  $\text{Mn}_3\text{O}_4$  surface is only partially covered. In the literature, ZSH generally

completely covers the surface of the cathode.<sup>[36,47]</sup> The edges of the  $\text{Mn}_3\text{O}_4$  deposits (within the gaps) likely act as preferential nucleation sites (larger surface area per unit volume) for ZSH formation, resulting in ZSH formation between the  $\text{Mn}_3\text{O}_4$  islands, rather than forming directly on top of the  $\text{Mn}_3\text{O}_4$  layer. Once the gaps between the  $\text{Mn}_3\text{O}_4$  islands have been filled with ZSH, further formation occurs across the surface of the  $\text{Mn}_3\text{O}_4$ .<sup>[49]</sup> The STEM image and EDX results reveal two different microstructural features. Mn oxide, with Zn incorporation/intercalation, is present (as in Figure 4a); however, there is a Zn–O–S rich phase (circled particles in Figure 4b) which correlates with the ZSH plates in the SEM image. These regions do not contain Mn and exhibit brighter contrast than Mn oxide in the STEM ADF image. It is generally agreed that ZSH plates form because of a change in the pH of the electrolyte from the formation of  $\text{MnOOH}$ ; however, the presence of  $\text{MnOOH}$  could not be confirmed in this work.<sup>[28,36,47]</sup>

Similar analyses were done for the first charge point (1.54 V) and the second charge point (1.63 V) during the conditioning cycle (Figure 4c and 4d, respectively). The morphology of the cathode resembles that of the as deposited sample and most of the ZSH plates have dissolved at the first charge point. The STEM/EDX analysis shows that some ZSH is still present on the surface of the cathode (Figure 4c). In fact, a Mn oxide particle is covered by ZSH. For the 1.63 V sample, the ZSH plates have completely dissolved (Figure 4d). The morphology of the sample is very similar to the as deposited  $\text{Mn}_3\text{O}_4$ . Zn is still present within the Mn oxide after the electrode is almost fully charged. This may be due to a phase change of  $\text{Mn}_3\text{O}_4$  to  $\text{ZnMn}_2\text{O}_4$  (which has a crystal structure very similar to hausmannite  $\text{Mn}_3\text{O}_4$ ) during the discharge portion of the conditioning cycle<sup>[19,36,47]</sup> and may account for the different shape of the GCD curves during subsequent cycles. It should be noted that some S remains in the Mn oxide (or  $\text{ZnMn}_2\text{O}_4$ ) and is likely from the fabrication process, as previously discussed.

Microstructural analysis was done for the 1st cycle (Figure 5) and the 5th cycle (Figure S5) after conditioning. The positions selected correspond to the ends of the first and second plateaus. The cathode material at the first point of discharge (1.54 V) of the 1st cycle (Figure 5a) has a morphology similar to the first point of discharge during the conditioning cycle (Figure 4a). Mn oxide particles, with Zn intercalation and some S, are present; no ZSH plates were detected. At the second point of discharge (1.25 V, Figure 5b), ZSH plates reappear; one



**Figure 4.** SEM SE images, STEM ADF images, and STEM EDX maps for the conditioning cycle at different points along discharge and charge: a) discharge point 1 (1.35 V), b) discharge point 2 (1.25 V) with arrows indicating ZSH plates, c) charge point 1 (1.54 V), and d) charge point 2 (1.63 V). The circled particles in b) indicate the Zn–S–O rich particles. The maps shown in the bottom righthand corner for each potential are overlays of Mn, O, Zn, and S. The inset GCD plots depict the positions along the cycle where the battery was stopped for analysis.

such plate is shown in the STEM image and EDX maps. An electron diffraction pattern was obtained from the ZSH plate in Figure 5b and was indexed to ZSH (Figure S6 and Table S1), confirming that the plates are indeed ZSH. Additionally, less ZSH is formed when compared with the conditioning cycle discharge. The lower amount of ZSH correlates with a smaller second discharge plateau for the first cycle after conditioning relative to the second discharge plateau for the conditioning cycle. Furthermore, the reduced formation of ZSH after the conditioning cycle may account for the excellent GCD perform-

ance of the battery, since ZSH formation on the cathode surface has been described as detrimental to cyclability.<sup>[47]</sup> Combining the GITT results for the 1st cycle after conditioning with the electron microscopy results, ZSH formation during the second plateau is confirmed and its formation is most likely kinetically limited.<sup>[36,47]</sup> Similar electron microscopy results were obtained for the 5th cycle after conditioning and are presented in Figure S5. Figure 5c and 5d show the two different charge points at the end of each charge plateau (1.54 and 1.63 V) for the 1st cycle after conditioning. The results shown are similar

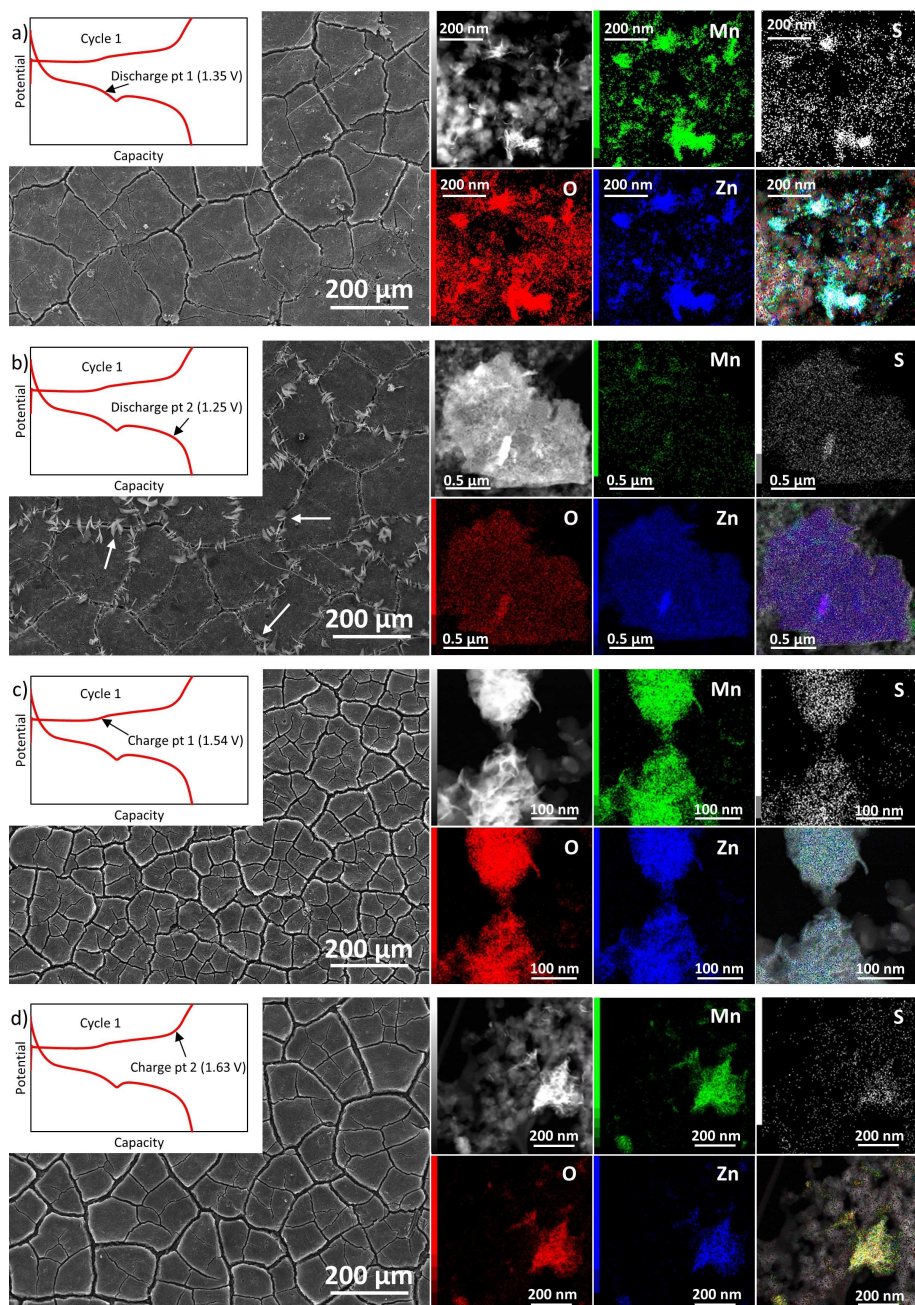


**Figure 5.** SEM SE images, STEM ADF images, and STEM EDX maps for the 1st cycle after conditioning at different points along discharge and charge: a) discharge point 1 (1.54 V), b) discharge point 2 with the arrows indicating ZSH plates (1.25 V), c) charge point 1 (1.54 V), and d) charge point 2 (1.63 V). The maps shown in the bottom right-hand corner for each potential are overlays of Mn, O, Zn, and S. The inset GCD plots depict the positions along the cycle where the battery was stopped for analysis.

to those for the conditioning cycle. The ZSH plates have dissolved by the end of the 1st plateau and the morphology is similar to that for the as deposited sample. The Mn oxide particles still contain Zn and some S. Although the GCD curves for the conditioning cycle and first cycle after conditioning are different, the results from SEM and STEM EDX are very similar. This further supports the proposed transformation of  $\text{Mn}_3\text{O}_4$  to  $\text{ZnMn}_2\text{O}_4$  during the conditioning cycle discharge. The electron microscopy results for the 5th charge cycle after conditioning

are similar to those for the 1st charge cycle and are presented in Figure S5.

Fully charged (1.8 V) and discharged (1.0 V) samples after the conditioning cycle and the 5th cycle after conditioning were examined using XPS. The XPS data is summarized in Table 3. For the fully discharged conditioning cycle, there are intense Zn 2p peaks and quantification shows a significant increase in the amount of Zn, which supports Zn intercalation and the formation of ZSH during discharge (Figure 6a). The position of the S peak in the survey scan corresponds to  $\text{ZnSO}_4$ ,

**Table 3.** Summary of XPS data collected for as deposited  $Mn_3O_4$  cathode, cathode after the conditioning cycle, and cathode after the 5<sup>th</sup> cycle after conditioning.

	Mn (At%)	O (At%)	Zn (At%)	S (At%)	Mn 2p Avg Ox State	Mn 3s Splitting (eV)	Mn 2p (3/2)/ O 1s Difference (eV)	Zn LMM Kinetic Energy (eV)	O 1s (eV)	S 2p (eV)
Deposited $Mn_3O_4$	45.3	54.7	—	—	2.55	5.54	111.62	—	—	—
Conditioning discharge	8.8	52.1	31.1	8.0	—	—	—	987.7	531.5	168.6
Conditioning charge	43.9	53.6	2.5	—	2.54	5.47	111.55	989.5	529.5	—
5th discharge	9.1	52.8	31.7	6.3	—	—	—	988.0	531.0	168.0
5th charge	44.0	52.1	3.9	—	2.52	5.29	111.47	989.7	529.4	—
$Mn_3O_4^{[48]}$	42.9	57.1	—	—	2.67	5.5	111.53	—	—	—

possibly present as ZSH.<sup>[54]</sup> Additionally, the strong Mn peaks are significantly reduced in intensity (Mn 2p and Mn 3s peaks) and some peaks have completely disappeared (Mn LMM Auger and Mn 2s peaks) when compared with the pristine  $Mn_3O_4$  survey scan (Figure S1). The positions of the main O 1s peak and left shoulder, as well as the Zn (Auger) LMM peak, indicate that  $ZnSO_4$  and  $Zn(OH)_2$  are present on the cathode surface, most likely in the form of ZSH (Figure 6b and 6c).<sup>[55–57]</sup> The O 1s peak has a shoulder at 529.7 eV which indicates that metal oxide is also present on the surface, possibly in the form of  $ZnMn_2O_4$  (Figure 6b).<sup>[25,48,58]</sup> The oxidation state of the compound could not be reliably determined due to significant overlap of the Zn 3s peak and Mn 3p peaks, as well as the poor Mn 2p satellite feature signal because of the formation of ZSH on the surface of the cathode. After full charge for the conditioning cycle, the survey scan shows the return of the Mn 2s and Mn Auger peaks and a significant increase in intensity of the Mn 2p and Mn 3s peaks (Figure 6d). However, Zn 2p and Zn Auger peaks are still present, but reduced in intensity, indicating incomplete Zn extraction on charge. Additionally, the survey scan does not show any S, indicating that the ZSH has all been dissolved. The strong O 1s peak at 529.5 eV is associated with the presence of metal oxides, most likely in the form of  $ZnMn_2O_4$  (Figure 6e).<sup>[25,48,58]</sup> The small shoulder at 531.2 eV for the O 1s spectrum corresponds with surface adsorbed OH.<sup>[37,48,58]</sup> The change in the Zn LMM (Auger) peak shape and position (989.5 eV) on recharge indicates that a Zn containing oxide remains on charge, possibly in the form of  $ZnMn_2O_4$  (Figure 6f).<sup>[56,59]</sup> The Mn 2p satellite peak areas and Mn 3s peak splitting signify a return to a Mn spinel structure, further suggesting  $ZnMn_2O_4$  remains on recharge (Figure 6g and 6h).<sup>[25,58]</sup> The decrease in the Mn 3s peak splitting value compared with the pristine sample also indicates an increase in the average oxidation state of the Mn oxide (Table 3).<sup>[49]</sup> This supports the formation of  $ZnMn_2O_4$ ; as  $Mn^{2+}$  is replaced with  $Zn^{2+}$ , the average oxidation state of Mn would increase closer to 3. However, it is noted that there is significant overlap between the Mn 3s and Zn 3p peaks, which may reduce the accuracy of determining oxidation state from Mn 3s peak splitting.

The XPS results for the conditioning cycle, both charge and discharge, corroborate the electron microscopy results. Overall, the microstructural analysis for the conditioning cycle indicates that the difference in shape between conditioning cycle CV and

GCD curves and the curves for the subsequent cycles is likely due to a phase change from  $Mn_3O_4$  to  $ZnMn_2O_4$ .

The XPS data collected after full discharge for the 5th cycle after conditioning are similar to the results obtained after discharge for the conditioning cycle. The survey scan shows strong Zn 2p and Zn LMM Auger peaks and a marked reduction in intensity of the Mn peaks, indicating significant amounts of Zn incorporated in  $Mn_3O_4$  and/or forming ZSH during discharge (Figure 7a). The O 1s peak and shoulder at 531.0 eV and 532.3 eV, respectively, correlate with ZSH, while the shoulder at 529.4 eV suggests a metal oxide is also present (Figure 7b).<sup>[25,55,56]</sup> The Zn Auger peak position (988.0 eV) and shape suggests the formation of a Zn–S containing compound, possibly in the form of ZSH (Figure 7c).<sup>[54,56]</sup> XPS data for the 5th charge cycle after conditioning are also similar to the data for the conditioning charge cycle. The survey scan shows the return of the strong Mn peaks, but the Zn peaks (2p and Zn LMM) intensities are significantly reduced indicating that most of the Zn has been removed (Figure 7d). The position and shape of the O 1s peaks (Figure 7e) and the Zn Auger peaks (Figure 7f) indicate that a Zn containing oxide may be present on the cathode, possibly as  $ZnMn_2O_4$ .<sup>[25,58,59]</sup> The small shoulder at 531.2 of the O 1s peak is likely from surface adsorbed OH.<sup>[37,48,58]</sup> The oxidation state determined from Mn 2p satellite features (Figure 7g) and the Mn 3s peak splitting (Figure 7h) indicate a return to a Mn-based spinel, suggesting that  $ZnMn_2O_4$  remains on charge.<sup>[25,58]</sup> Furthermore, the Mn 3s peak splitting is shown to decrease further when compared with the conditioning cycle, indicating an increase in the oxidation state of the Mn oxide as it is cycled.<sup>[49]</sup> The increase is likely due to additional  $Mn^{2+}$  substitution by  $Zn^{2+}$ , further supporting the formation of  $ZnMn_2O_4$ . The XPS data also shows an increase in the amount of Zn for the 5th cycle versus the conditioning cycle, which supports the increase in Mn oxidation state due to Zn substitution and the formation of  $ZnMn_2O_4$  (Table 3). The XPS data for the 5th cycle after conditioning corroborates the electron microscopy results for both the 1st cycle after conditioning and the 5th cycle after conditioning.

Based on the electrochemical and microstructural characterization data for the conditioning cycle, the 1st cycle after conditioning, and the 5th cycle after conditioning, some insight can be provided regarding the reaction mechanism for the  $Mn_3O_4$ -based cathode. The results indicate a mechanism similar to that for  $ZnMn_2O_4$  proposed by Chen et al.<sup>[26]</sup> and somewhat similar to that for  $MnO_2$  proposed by Huang et al. and Yun

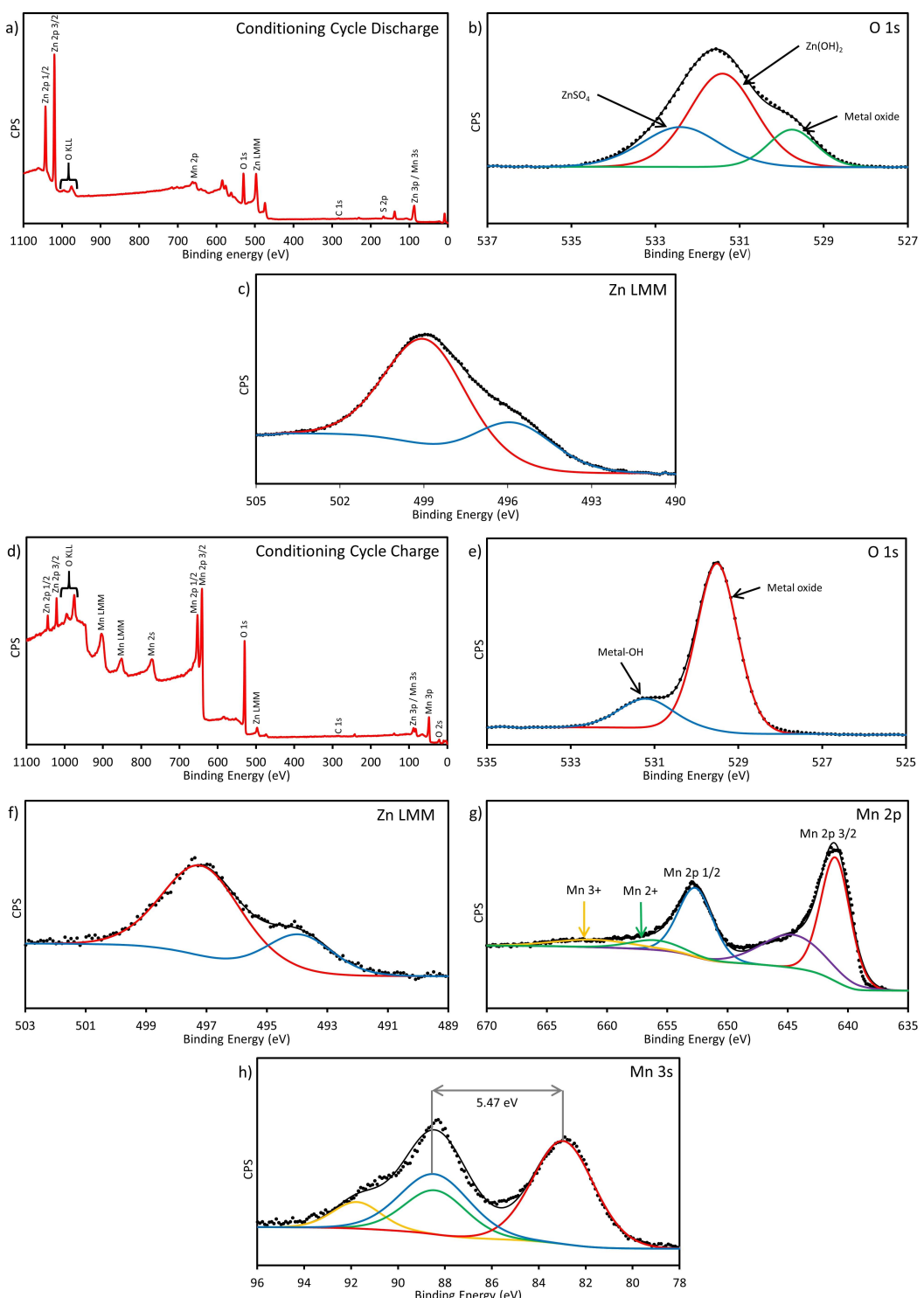


**Figure 6.** XPS results for the full conditioning cycle discharge (1.0 V) and charge (1.8 V): a) Discharge survey scan, b) discharge O 1s spectrum, c) discharge Zn Auger LMM peak, d) charge survey scan, e) charge O 1s spectrum, f) charge Zn Auger LMM spectrum, g) charge Mn 2p spectrum, and h) charge Mn 3s spectrum.

et al.<sup>[36,47]</sup> Overall, the proposed reaction mechanism can be summarized as follows. During the conditioning cycle discharge,  $Zn^{2+}$  and possibly  $H^+$  intercalation occur during the first plateau. This is followed by the formation of ZSH from Zn and S in the electrolyte during the second plateau. Further-

more, during the conditioning cycle, the  $Mn_3O_4$  cathode undergoes a phase transformation to  $ZnMn_2O_4$  as more  $Zn^{2+}$  is intercalated into the cathode. Both  $Mn_3O_4$  and  $ZnMn_2O_4$  have very similar crystal structures and lattice parameters, which facilitates the transformation. During the conditioning cycle

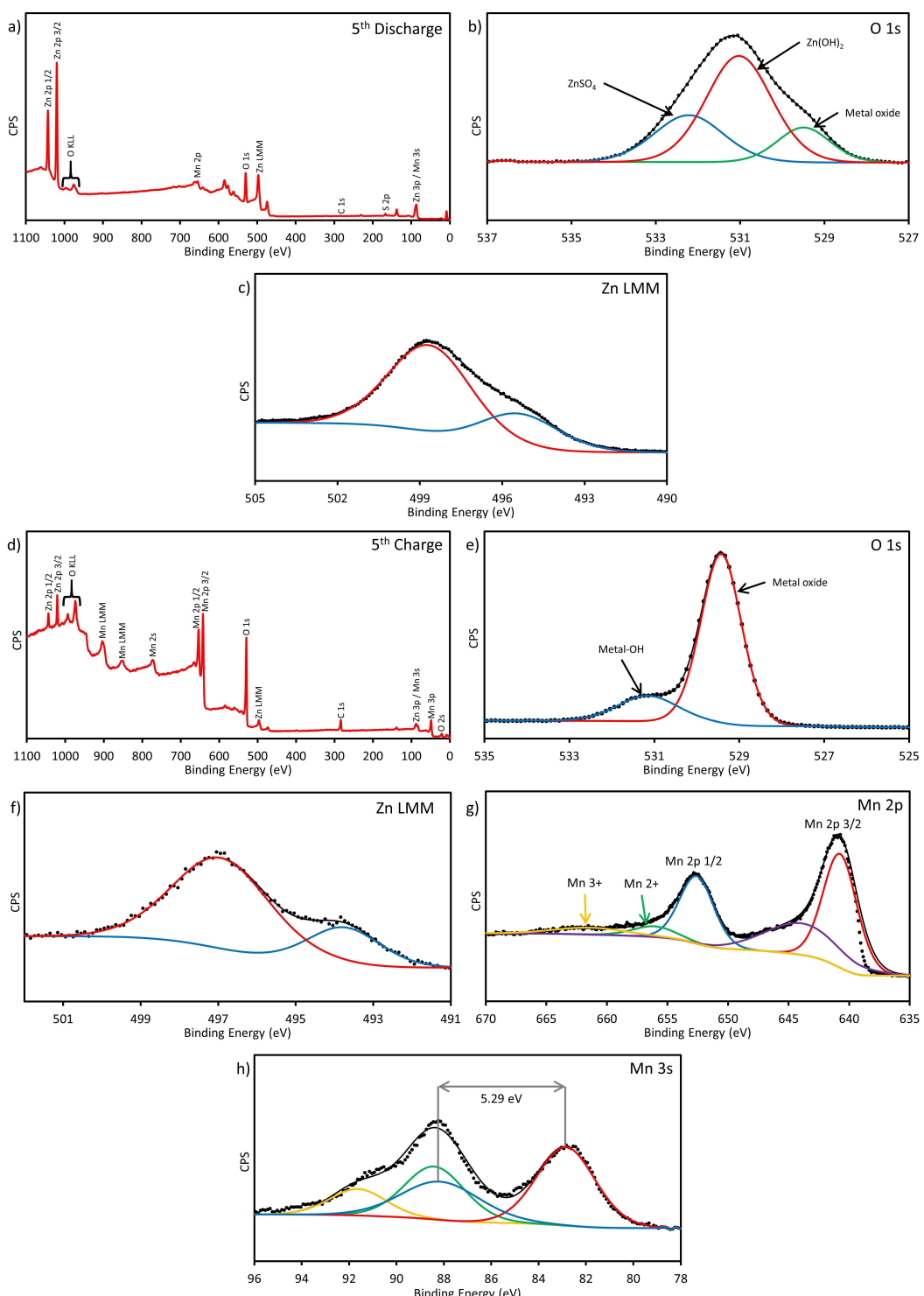


**Figure 7.** XPS results for the full discharge (1.0 V) and charge (1.8 V) of the 5<sup>th</sup> cycle after conditioning: a) Discharge survey scan, b) discharge O 1s spectrum, c) discharge Zn Auger LMM spectrum, d) charge survey scan, e) charge O 1s spectrum, f) charge Zn Auger LMM spectrum, g) charge Mn 2p spectrum, and h) charge Mn 3s spectrum.

charge, ZSH is dissolved during the first charge plateau and  $Zn^{2+}$  (and  $H^+$  if present) ions are extracted from the cathode curing the second charge plateau. However, a finite amount of Zn is not extracted and remains, most likely as  $ZnMn_2O_4$  from the initial phase transformation. During subsequent discharge cycles after conditioning, the formed  $ZnMn_2O_4$  will intercalate

$Zn^{2+}$  (and possibly  $H^+$ ) ions during the first plateau. ZSH again forms during the second plateau. On charge, ZSH will dissolve during the first plateau and most of the  $Zn^{2+}$  (and  $H^+$ ) ions are extracted during the second plateau. This analysis indicates a reaction mechanism different from what has been previously proposed for  $Mn_3O_4$  and other Mn spinels used for ZIBs

cathodes. Other  $\text{Mn}_3\text{O}_4$  mechanisms propose only  $\text{H}^+$  intercalation during the first plateau, with  $\text{Zn}^{2+}$  intercalation and ZSH formation in the second.<sup>[31,32]</sup> This work clearly shows that Zn is present in the Mn oxide during the first plateau on both charge and discharge. Additionally, other proposed  $\text{Mn}_3\text{O}_4$  mechanisms involve a phase change to  $\text{MnO}_2$  or  $\text{MnO}$  while this work proposes the transformation of  $\text{Mn}_3\text{O}_4$  to  $\text{ZnMn}_2\text{O}_4$ .  $\text{ZnMn}_2\text{O}_4$  spinel structures are generally proposed to undergo only Zn intercalation within both plateaus, without the formation of ZSH, while this work clearly shows ZSH forms during the second plateau.<sup>[24,25]</sup> However, further tests and analysis are needed to further elucidate the mechanism(s) for charge and discharge of  $\text{Mn}_3\text{O}_4$ .

### 3. Conclusions

Nanocrystalline  $\text{Mn}_3\text{O}_4$  cathodes for Zn-ion batteries (ZIBs) were fabricated by simple pulsed electrodeposition onto carbon paper (CP). Electrodeposition offers several advantages including the elimination of binders, room temperature deposition, and very short fabrication times. The maximum capacity for a ZIB using electrodeposited  $\text{Mn}_3\text{O}_4$  as the cathode was  $376 \text{ mAh g}^{-1}$ . The battery was able to achieve a capacity retention of 139% after 200 cycles at a current density of  $1 \text{ A g}^{-1}$ . The fabricated electrode also showed excellent rate capability performance with capacities of 201, 180, 164, 143, and  $217 \text{ mAh g}^{-1}$  at current densities of 300, 600, 1200, 2400, and again at  $300 \text{ mA g}^{-1}$ , respectively. The excellent battery performance of the  $\text{Mn}_3\text{O}_4$  is proposed to be a result of several different factors: the crystal structure of the deposited oxide, its oxide morphology and thickness, limited formation of ZSH only within  $\text{Mn}_3\text{O}_4$  cracks during cycling, and the CP substrate providing good electronic conductivity. Through a combination of microstructural analysis, using electron microscopy and X-ray photoelectron spectroscopy, and electrochemical testing, additional insight into the reaction mechanisms has been obtained and points to a two-step reaction mechanism for ZIBs using  $\text{Mn}_3\text{O}_4$  cathodes. The first discharge potential plateau during discharge likely involves intercalation of  $\text{Zn}^{2+}$  and possibly  $\text{H}^+$ , followed by a conversion reaction forming ZSH during the second discharge potential plateau. The reverse occurs on charge.

### Acknowledgements

The authors are grateful to the Natural Sciences and Engineering Research Council (NSERC RGPIN-2018-04488) of Canada for research funding. The authors would also like to acknowledge the contributions and support from Michael Clark, Yi Shen, and Shiraz Merali.

### Conflict of Interest

The authors declare no conflict of interest.

**Keywords:** electrodeposition • electron microscopy • manganese oxide • transition metals • zinc-ion batteries

- [1] J. Ming, J. Guo, C. Xia, W. Wang, H. N. Alshareef, *Mater. Sci. Eng. R* **2019**, *135*, 58–84.
- [2] J. Liu, C. Xu, Z. Chen, S. Ni, Z. X. Shen, *Green Energy Environ.* **2017**, *3*, 1, 20–41.
- [3] R. Guduru, J. Icaza, *Nanomaterials* **2016**, *6*, 41.
- [4] M. Song, H. Tan, D. Chao, H. J. Fan, *Adv. Funct. Mater.* **2018**, *28*, 1802564.
- [5] G. Fang, J. Zhou, A. Pan, S. Liang, *ACS Energy Lett.* **2018**, *3*, 2480–2501.
- [6] D. Chao, C. (Rose) Zhu, M. Song, P. Liang, X. Zhang, N. H. Tiep, H. Zhao, J. Wang, R. Wang, H. Zhang, H. J. Fan, *Adv. Mater.* **2018**, *30*, 1–7.
- [7] D. Kundu, B. D. Adams, V. Duffort, S. H. Vajargah, L. F. Nazar, *Nat. Energy* **2016**, *1*, 16119.
- [8] T. Wei, Q. Li, G. Yang, C. Wang, *Electrochim. Acta* **2018**, *287*, 60–67.
- [9] X. Chen, L. Wang, H. Li, F. Cheng, J. Chen, *J. Energy Chem.* **2019**, *38*, 20–25.
- [10] J. Shin, D. S. Choi, H. J. Lee, Y. Jung, J. W. Choi, *Adv. Energy Mater.* **2019**, *1900083*, 1–11.
- [11] M. Yan, P. He, Y. Chen, S. Wang, Q. Wei, K. Zhao, X. Xu, Q. An, Y. Shuang, Y. Shao, K. T. Mueller, L. Mai, J. Liu, J. Yang, *Adv. Mater.* **2018**, *30*, 1–6.
- [12] J. Ding, Z. Du, L. Gu, B. Li, L. Wang, S. Wang, Y. Gong, *Adv. Mater.* **2018**, *30*, 1800762, 1–6.
- [13] B. Tang, G. Fang, J. Zhou, L. Wang, Y. Lei, C. Wang, T. Lin, Y. Tang, S. Liang, *Nano Energy* **2018**, *51*, 579–587.
- [14] F. Wan, L. Zhang, X. Dai, X. Wang, Z. Niu, J. Chen, *Nat. Commun.* **2018**, *9*, 1656–1667.
- [15] R. Trócoli, F. La Mantia, *ChemSusChem* **2015**, *8*, 481–485.
- [16] L. Zhang, L. Chen, X. Zhou, Z. Liu, *Sci. Rep.* **2015**, *5*, 1–11.
- [17] Z. Liu, P. Bertram, F. Endres, *J. Solid State Electrochem.* **2017**, *21*, 2021–2027.
- [18] Z. Jia, B. Wang, Y. Wang, *Mater. Chem. Phys.* **2015**, *149*, 601–606.
- [19] M. H. Alfaruqi, V. Mathew, J. Gim, S. Kim, J. Song, J. P. Baboo, S. H. Choi, J. Kim, *Chem. Mater.* **2015**, *27*, 3609–3620.
- [20] M. H. Alfaruqi, S. Islam, D. Y. Putro, V. Mathew, S. Kim, J. Jo, S. Kim, Y. K. Sun, K. Kim, J. Kim, *Electrochim. Acta* **2018**, *276*, 1–11.
- [21] N. Palaniandy, M. A. Kebede, K. Raju, K. I. Ozoemena, L. le Roux, M. K. Mathe, R. Jayaprakasam, *Mater. Chem. Phys.* **2019**, *230*, 258–266.
- [22] M. H. Alfaruqi, S. Islam, J. Gim, J. Song, S. Kim, D. T. Pham, J. Jo, Z. Xiu, V. Mathew, J. Kim, *Chem. Phys. Lett.* **2016**, *650*, 64–68.
- [23] C. Guo, H. Liu, J. Li, Z. Hou, J. Liang, J. Zhou, Y. Zhu, Y. Qian, *Electrochim. Acta* **2019**, *304*, 370–377.
- [24] N. Zhang, F. Cheng, Y. Liu, Q. Zhao, K. Lei, C. Chen, X. Liu, J. Chen, *J. Am. Chem. Soc.* **2016**, *138*, 12894–12901.
- [25] X. Wu, Y. Xiang, Q. Peng, X. Wu, Y. Li, F. Tang, R. Song, Z. Liu, Z. He, X. Wu, *J. Mater. Chem. A* **2017**, *5*, 17990–17997.
- [26] L. Chen, Z. Yang, H. Qin, X. Zeng, J. Meng, *J. Power Sources* **2019**, *425*, 162–169.
- [27] G. G. Yadav, J. Cho, D. Turney, B. Hawkins, X. Wei, J. Huang, S. Banerjee, M. Nyce, *Adv. Energy Mater.* **2019**, *1902270*.
- [28] H. Pan, Y. Shao, P. Yan, Y. Cheng, S. K. Han, Z. Nie, C. Wang, J. Yang, X. Li, P. Bhattacharya, K. T. Mueller, J. Liu, *Nat. Energy* **2016**, *1*, 16039.
- [29] C. Xu, B. Li, H. Du, F. Kang, *Angew. Chem. Int. Ed.* **2012**, *51*, 933–935; *Angew. Chem.* **2012**, *124*, 957–959.
- [30] W. Sun, F. Wang, S. Hou, C. Yang, X. Fan, Z. Ma, T. Gao, F. Han, R. Hu, M. Zhu, C. Wang, *J. Am. Chem. Soc.* **2017**, *139*, 9775–9778.
- [31] J. Hao, J. Mou, J. Zhang, L. Dong, W. Liu, C. Xu, F. Kang, *Electrochim. Acta* **2018**, *259*, 170–178.
- [32] C. Zhu, G. Fang, J. Zhou, J. Guo, Z. Wang, C. Wang, J. Li, Y. Tang, S. Liang, *J. Mater. Chem. A* **2018**, *6*, 9677–9683.
- [33] S. Khamsanga, R. Pornprasertsuk, T. Yonezawa, A. A. Mohamad, S. Kheawhom, *Sci. Rep.* **2019**, *9*, 8441.
- [34] S. Yang, M. Zhang, X. Wu, X. Wu, F. Zeng, Y. Li, S. Duan, D. Fan, Y. Yang, X. Wu, *J. Electroanal. Chem.* **2019**, *832*, 69–74.
- [35] N. Zhang, F. Cheng, J. Liu, L. Wang, X. Long, X. Liu, F. Li, J. Chen, *Nat. Commun.* **2017**, *8*, 405.
- [36] Y. Huang, J. Mou, W. Liu, X. Wang, L. Dong, F. Kang, C. Xu, *Nano-Micro Lett.* **2019**, *11*, 49.
- [37] M. Xiong, M. P. Clark, M. Labbe, D. G. Ivey, *J. Power Sources* **2018**, *393*, 108–118.
- [38] D. Aasen, M. Clark, D. G. Ivey, *Batteries* **2019**, *2*, 1–13.

- [39] G. Fang, C. Zhu, M. Chen, J. Zhou, B. Tang, X. Cao, X. Zheng, A. Pan, S. Liang, *Adv. Funct. Mater.* **2019**.
- [40] M. H. Alfaruqi, J. Gim, S. Kim, J. Song, J. Jo, S. Kim, V. Mathew, J. Kim, *J. Power Sources* **2015**, *288*, 320–327.
- [41] M. H. Alfaruqi, J. Gim, S. Kim, J. Song, D. T. Pham, J. Jo, Z. Xiu, V. Mathew, J. Kim, *Electrochem. Commun.* **2015**, *60*, 121–125.
- [42] B. Wu, G. Zhang, M. Yan, T. Xiong, P. He, L. He, X. Xu, L. Mai, *Small* **2018**, *14*, 1–8.
- [43] V. Soundharajan, B. Sambandam, S. Kim, V. Mathew, J. Jo, S. Kim, J. Lee, S. Islam, K. Kim, Y. K. Sun, J. Kim, *ACS Energy Lett.* **2018**, *3*, 1998–2004.
- [44] D. Chao, W. Zhou, C. Ye, Q. Zhang, Y. Chen, L. Gu, K. Davey, S. Z. Qiao, *Angew. Chem. Int. Ed.* **2019**, *58*, 7823–7828.
- [45] G. H. A. Therese, P. V. Kamath, *Chem. Mater.* **2000**, *12*, 1195–1204.
- [46] G. Sun, X. Jin, H. Yang, J. Gao, L. Qu, *J. Mater. Chem. A* **2018**, *6*, 10926–10931.
- [47] Y. Li, S. Wang, J. R. Salvador, J. Wu, B. Liu, W. Yang, J. Yang, W. Zhang, J. Liu, J. Yang, *Chem. Mater.* **2019**, *31*, 2036–2047.
- [48] M. Chigane, M. Ishikawa, *J. Am. Chem. Soc.* **2000**, *147*, 2246–2251.
- [49] M. Clark, D. G. Ivey, *Nanotechnology* **2015**, *26*, 384001.
- [50] T. Gao, H. Fjellvåg, P. Norby, *Anal. Chim. Acta* **2009**, *648*, 235–239.
- [51] J. Jiang, A. Kucernak, *Electrochim. Acta* **2002**, *47*, 2381–2386.
- [52] J. Wang, J. G. Wang, H. Liu, C. Wei, F. Kang, *J. Mater. Chem. A* **2019**, *7*, 13727–13735.
- [53] D. Xu, B. Li, C. Wei, Y. B. He, H. Du, X. Chu, X. Qin, Q. H. Yang, F. Kang, *Electrochim. Acta* **2014**, *133*, 254–261.
- [54] R. V. Siriwardane, J. A. Poston, *Appl. Surf. Sci.* **1990**, *45*, 131–139.
- [55] G. Deroubaix, P. Marcus, *Surf. Interface Anal.* **1992**, *18*, 39–46.
- [56] B. R. Strohmeier, D. M. Hercules, *J. Catal.* **1984**, *86*, 266–279.
- [57] V. I. Nefedov, *J. Electron Spectrosc. Relat. Phenom.* **1982**, *25*, 29–47.
- [58] N. Guo, X. Q. Wei, X. L. Deng, X. J. Xu, *Nanoscale Res. Lett.* **2015**, *356*, 1127–1134.
- [59] M. C. Biesinger, B. P. Payne, A. P. Grosvenor, L. W. M. Lau, A. R. Gerson, R. S. C. Smart, *Appl. Surf. Sci.* **2011**, *257*, 2717–2730.

Manuscript received: October 9, 2019

Revised manuscript received: December 1, 2019

Version of record online: December 27, 2019